

Supporting Information for

Rationally Designed Surface Microstructural Features for Enhanced Droplet Jumping and Anti-frosting Performance

Guanlei Zhao^{ab}, Guisheng Zou^a, Wengan Wang^a, Ruikun Geng^a, Xiao Yan^d, Zhiyuan He^b, Lei Liu^{a}, Xin Zhou^e, Jianyong Lv^{b*}, Jianjun Wang^{b,c*}*

- a. Department of Mechanical Engineering, State Key Laboratory of Tribology, Key Laboratory for Advanced Manufacturing by Materials Processing Technology, Ministry of Education of PR China, Tsinghua University, Beijing 100084, China.
- b. Institute of Chemistry, Chinese Academy of Sciences, Beijing 100190, China.
- c. School of Future Technology, University of Chinese Academy of Sciences, Beijing 100190, China.
- d. Institute of Nuclear and New Energy Technology, Tsinghua University, Beijing, 10084, China.
- e. School of Physical Sciences, University of Chinese Academy of Sciences, Beijing 100190, China

KEYWORDS: superhydrophobic, anti-frosting, droplet jumping, ultrafast laser processing, hierarchical structure

Supporting Videos

Video S1. Illustrative recording for the procedure to measure advancing and receding contact angle of a sessile droplet.

Video S2. Self-propelled jumping of condensed microdroplets through coalescence.

Video S3. 100 minutes condensation experiment on MCS20, the accumulated water amount saturates after around 20 minutes without obvious increase in water accumulation over time.

Video S4. Droplets coalesce and jump on MCS20 without size mismatch (duration: 18 ms).

Video S5. Droplet coalesce and jump on MCS20 with a size mismatch of 1.5 (duration: 12 ms).

Video S6. Single droplet self-transport from within the micro-cone diverging track to the top (duration: 2 ms).

Video S7. Multiple droplets coalescence event, which is visually different from single droplet self-transport (duration: ~0.7 ms).

Video S8. Side view of a droplet growing out of the micro-cone diverging track (MCS100) and eventually suspend on top (duration: 9 s).

Supporting Tables

Table S1. Calibration of results from image recognition algorithm.

Calibration test #	Forward subtraction (g/m²)	Manual counting (g/m²)	Discrepancy (%)	Reverse subtraction (g/m²)	Calibrated results (g/m²)	New discrepancy (%)
NS-1	0.160	0.106	50.9	0.070	0.090	17.8
NS-2	0.151	0.136	11.0	0.038	0.133	20.4
NS-3	0.102	0.084	21.4	0.024	0.078	7.7
MCS10-1	0.442	0.368	20.1	0.037	0.405	10.1
MCS10-1	0.242	0.213	13.6	0.042	0.200	6.1
MCS10-1	0.253	0.217	16.6	0.023	0.230	6.0
MCS20-1	0.392	0.337	16.3	0.050	0.342	1.5
MCS20-1	0.278	0.241	15.4	0.047	0.231	4.1
MCS20-1	0.29	0.269	7.8	0.032	0.258	4.3
MCS40-1	0.326	0.213	53.1	0.124	0.202	5.4
MCS40-1	0.321	0.232	38.4	0.099	0.222	4.5
MCS40-1	0.345	0.241	43.2	0.072	0.273	11.7
MCS60-1	0.366	0.257	42.4	0.100	0.266	3.4
MCS60-1	0.259	0.218	18.8	0.047	0.212	2.8
MCS60-1	0.236	0.182	29.7	0.029	0.207	12.1
MCS100-1	0.144	0.097	48.5	0.040	0.104	6.7
MCS100-1	0.188	0.108	74.1	0.071	0.117	7.7
MCS100-1	0.358	0.322	11.2	0.040	0.318	1.3

Table S2. Water removal efficiency of the prepared samples.

Sample	NS	MCS10	MCS20	MCS40	MCS60	MCS100
Removed Water Amount (g/m²)	3.42	12.72	13.91	13.02	9.11	5.58
Condensed Water Amount (g/m²)	11.97	17.88	17.46	17.00	17.11	16.32

Water Removing Efficiency (%)	28.58	71.14	79.63	76.58	53.27	34.17
--------------------------------------	-------	-------	-------	-------	-------	-------

S1. Surface Fabrication and Characterization

The Gaussian spot diameter of the laser used in this work is around $17.5\ \mu\text{m}$, and laser direct writing technique can be used to construct the microstructures of MCS10 and MCS20 by utilizing the threshold effect of ultrafast laser.¹ However, the microstructural features of MCS40, MCS60 and MCS100 are notably larger than the laser spot diameter. As a result, multiple laser scan per scan cycle is employed to fabricate micro-cone structures with larger structural scale. As shown in Figure S1, in the first scan cycle, the laser beam inscribes a microgroove with top opening of similar width as the laser beam diameter ($\sim 17.5\ \mu\text{m}$ diameter). In the second scan cycle, three consecutive laser beams spaced $5\ \mu\text{m}$ apart scan the same location, which results in larger microgroove. Then, in the third scan cycle, five consecutive laser beams scan the surface in a similar manner as the second scan. This process continues until the desired microgroove dimensions are achieved.

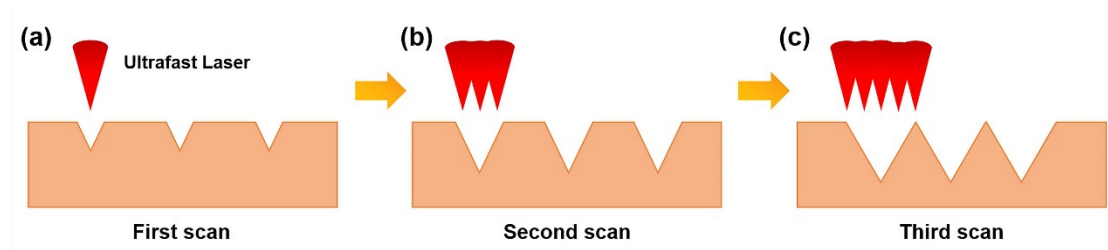


Figure S1. Schematic illustration shows the multi-scan fabrication process of MCS40, MCS60 and MCS100.

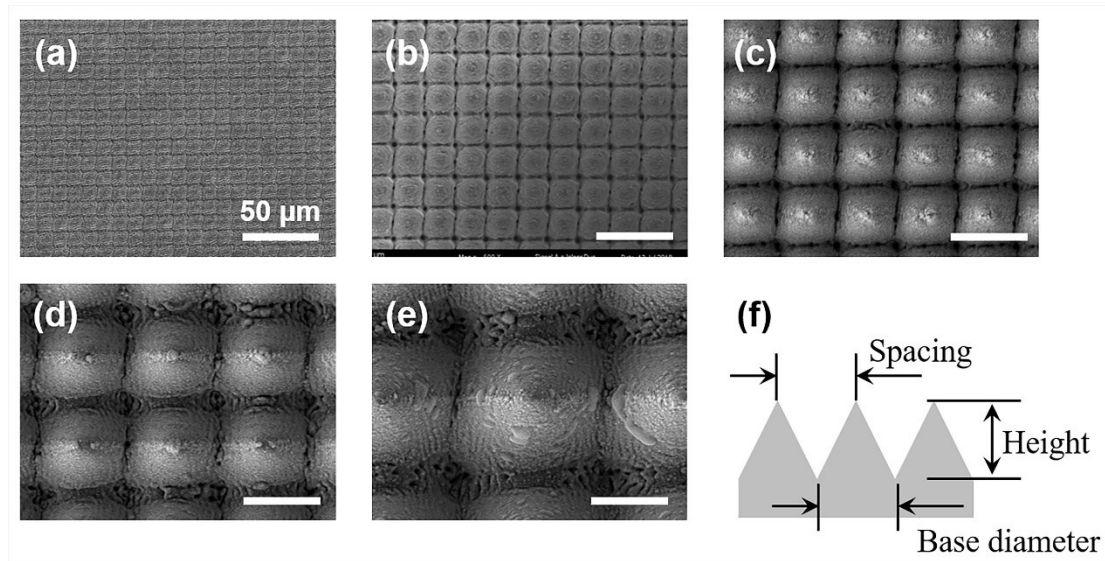


Figure S2. Top view of the SEM images for (a-e) MCS10, MCS20, MCS40, MCS60 and MCS100. (f) Definitions of the geometrical parameters for the SHSs.

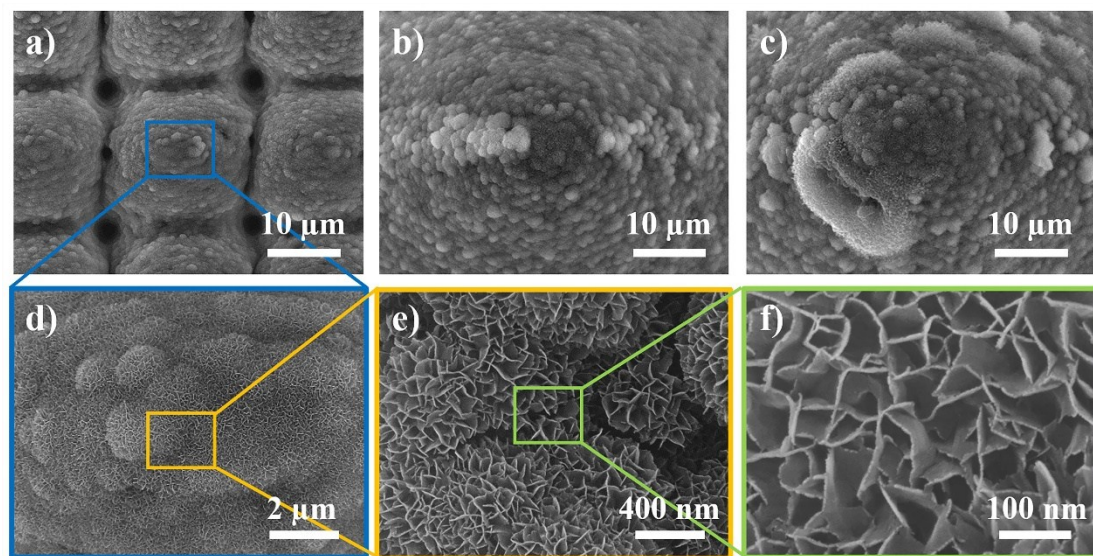


Figure S3. Magnified top view of the SEM images for (a) MCS20, (b) MCS60, and (c) MCS100. (d) Laser fabrication results in ubiquitous micro-roughness of 1-2 μm. (e-f) Magnified images show that nanostructure is ubiquitously formed onto the micro-cones, and the size scale of the nano-blades are at least two orders of magnitude smaller than the smallest micro-cone.

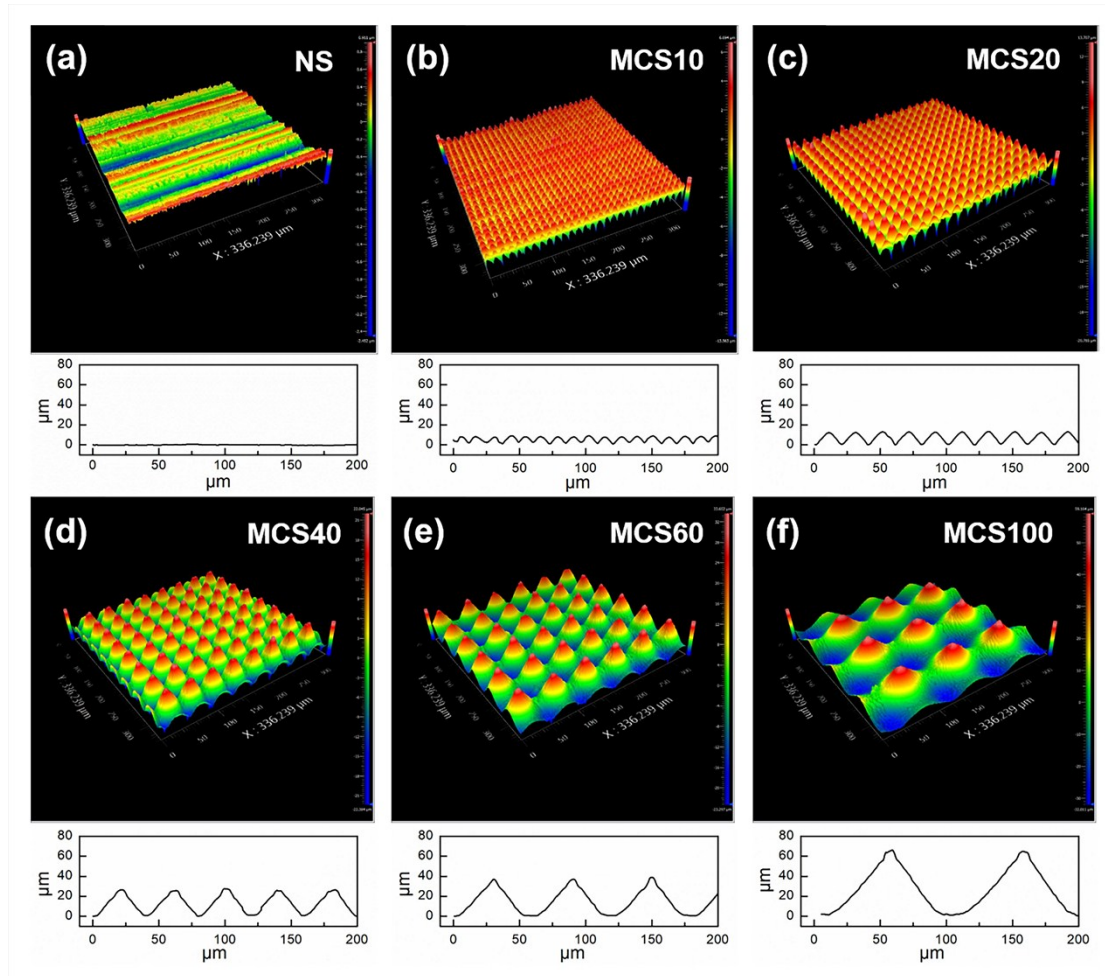


Figure S4. White light interferometry images of the SHSs. (a-f) White light interferometry images for NS, MCS10, MCS20, MCS40, MCS60 and MCS100. The heights of the micro-cones are measured and are shown in Table 1. The surface area of the SHSs are also evaluated using white light interferometry, and the normalized values with respect to NS are also shown in Table 1.

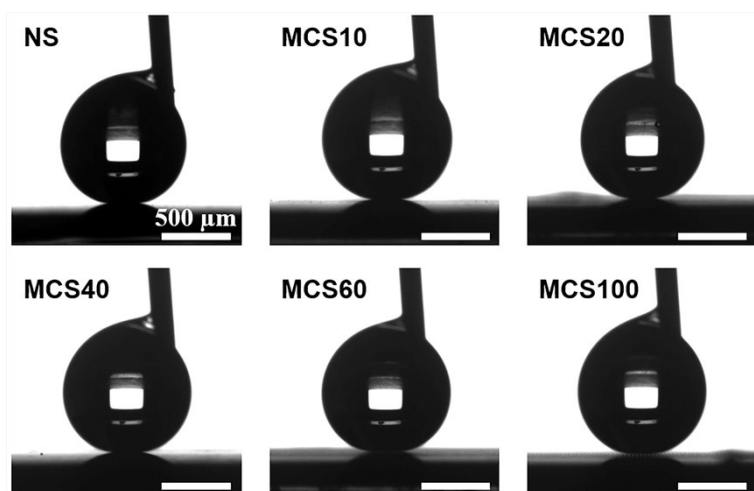


Figure S5. Advancing and receding contact angle measurements for the SHSs using the sessile droplet method (3.5 μL), the values are shown in Table 2. The snapshots were taken for advancing contact angle.

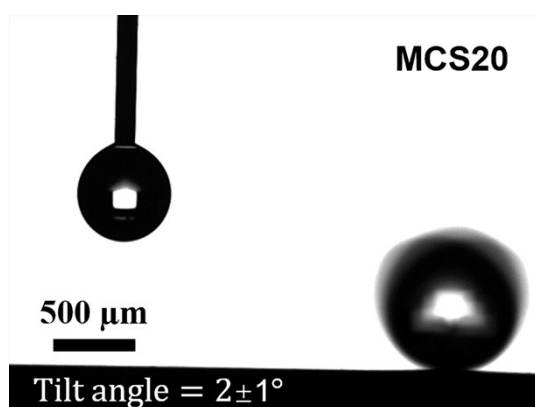


Figure S6. Representative snapshot of a 3.5 μL droplet rolling down on MCS20 at a tilting angle of $2\pm 1^\circ$.

S2. Condensation Experiment.

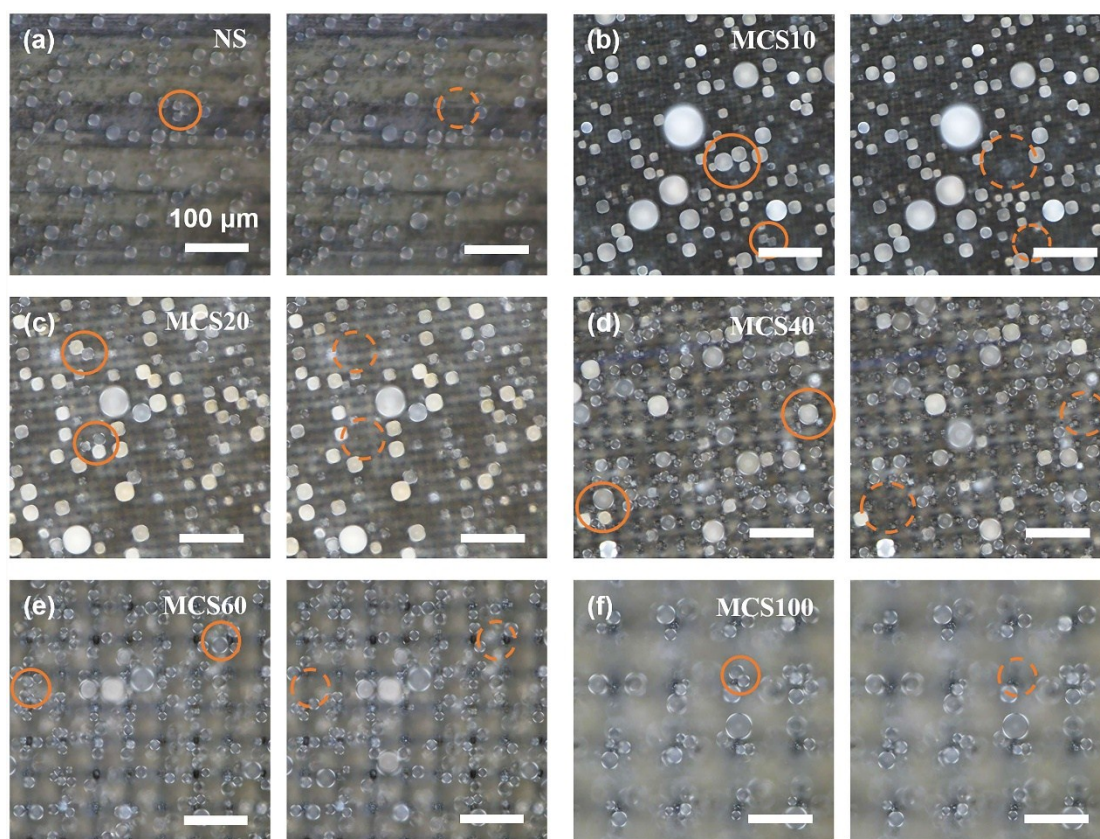


Figure S7. High resolution images illustrating droplet jumping phenomenon for (a) NS, (b) MCS10, (c) MCS20, (d) MCS40, (e) MCS60 and (f) MCS100. The images were taken using a multipurpose zoom microscope (Nikon AZ100). High quality images were obtained through adjusting the opening size of the aperture, illumination intensity, and focus.

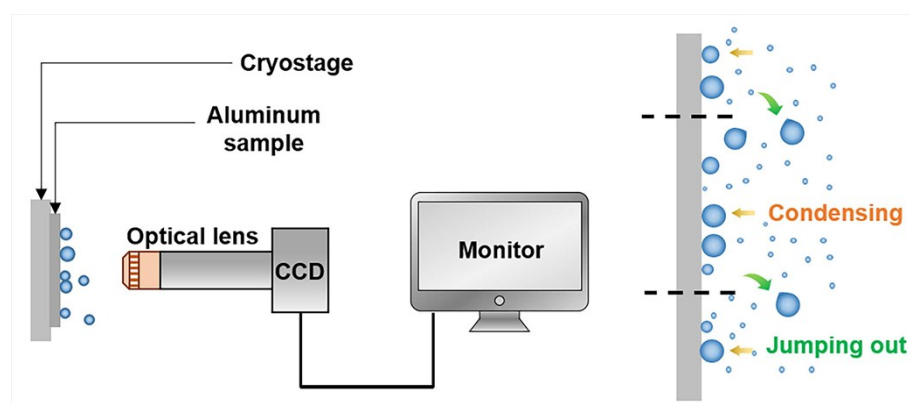


Figure S8. Schematic illustration of the setup for vertically investigating condensation

process. Samples were bonded with thermal paste onto a vertically oriented cryostage with ambient temperature and relative humidity of 25.3 ± 2.5 °C and $55.1 \pm 2.0\%$, respectively. The temperature of the cryostage were accurately controlled to be 1 ± 1.0 °C, which corresponds to an SSD of 2.71. An optical system with a mounted high-speed video camera was used to record the condensation process.

S3. Condensation Experiment Results Summary

Three condensation tests were conducted on each of the six different SHSs to obtain 18 condensation test results. Each test was recorded at 10 fps for 10 minutes, resulting in 6000 images per test. The dimension of observing view was $1.6 \text{ mm} \times 1.2 \text{ mm}$. It is challenging to estimate the amount of removed water from the condensation tests in an accurate and efficient manner. Manual counting using software such as Nanomeasure and ImageJ are usually time consuming and prone to human error. In this work, a shape detection algorithm was developed using MATLAB, and it significantly improved the efficiency and accuracy of data processing. The algorithm works as follows:

Figure S9a-b show two images of the condensation process which were taken in consecutive frames, the circled brighter looking droplets from the first image coalesce and jump off the surface, leaving a relatively darker background. Subtracting frame 1 by frame 2 (defined here as forward subtraction), along with image processing techniques such as binarizing and thresholding to enhance image contrast, the removed droplets between the two frames can be clearly seen in Figure S9c. Lastly, a circle detection algorithm was implemented to recognize all the round objects from Figure S9c, as shown in Figure S9d. The returned values of the algorithm are the number of droplets detected and their respective radii. By applying this technique for all 6000 images taken in the 10 minutes experiment, the amount of removed water in weight per centimeter square (by assuming spherical droplet shape. Sphere assumption should be reasonable for spherical cap at high contact angle, e.g. at 160° , the difference between

the volume of a sphere and a spherical cap is only 0.27%, which is negligible for our analysis), and the number of droplets removed during each condensation tests can be calculated using MS Excel and Visual Basic.

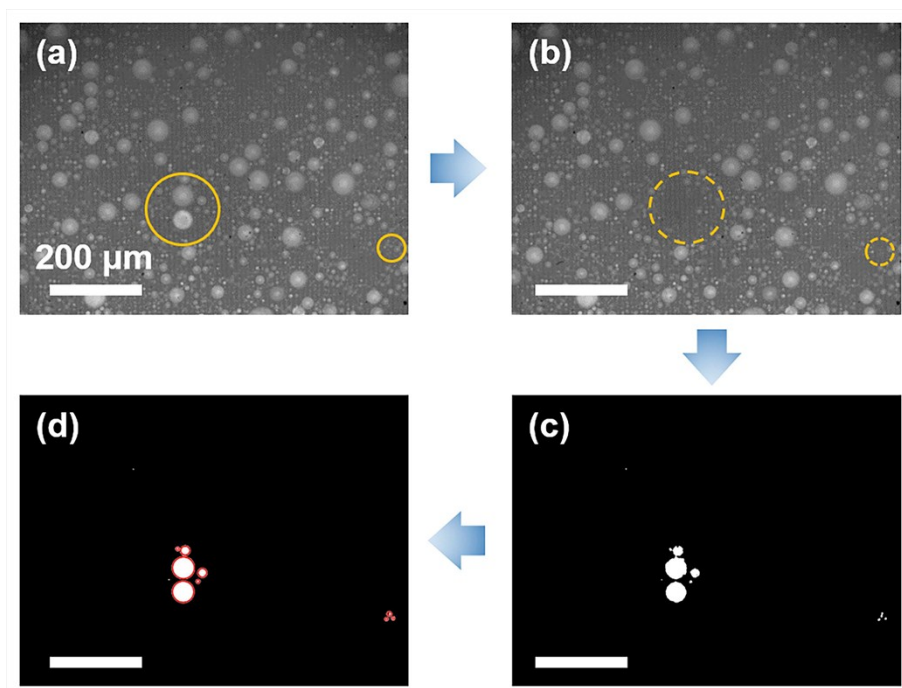


Figure S9. Data processing and calculation for amount of removed water for the SHSs.

To verify the feasibility of using the image recognition algorithm for counting the weight of removed droplets, we randomly selected 18 different sections from the recorded videos, each with 100 frames, and carefully counted the water removal amount manually using Nanomeasure. Disturbingly, the results obtained from image recognition algorithm always overestimated the water removal amount ($29.6 \pm 18.8\%$) as compared to manual counting, as shown in Table S1.

After close examination of the image recognition algorithm frame by frame, five factors that reduce the accuracy for droplet counting can be pinpointed. The first factor is high amplitude noise caused by a sudden motion of the experimental setup, shifting

the observing view for up to a few frames (e.g. hammering in construction sites outside of the laboratory). Such noise can be clearly seen on Figure S10a as huge spikes within the processed data, due to large quantities of recognized circles which are not removed droplets (Figure S10b). This problem can only be solved through locating and removing of the frames manually. For instance, 44 out of 6000 frames were removed for the first MCS20 condensation experiment, and improved accuracy can be obtained, as shown in Figure S10c.

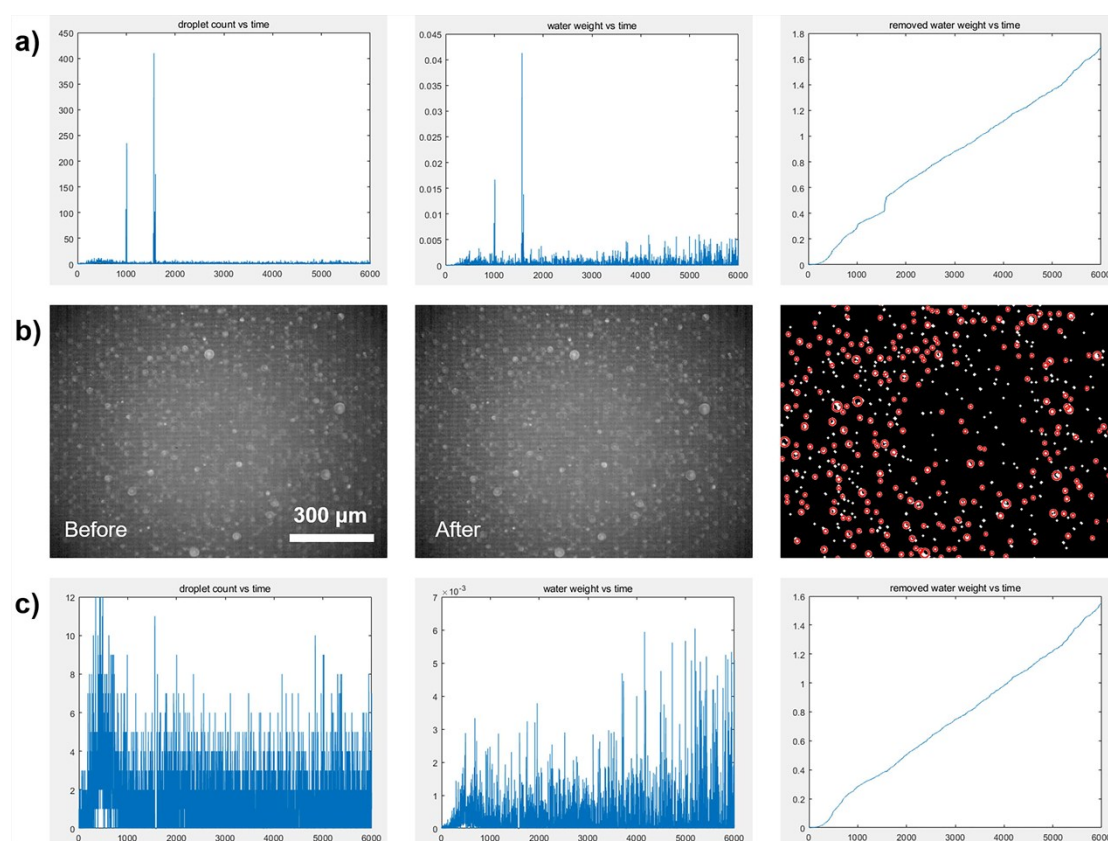


Figure S10. Elimination of high amplitude noise. (a) Raw data for recognized droplet number and weight with respect to frame number, the spikes show the frames where high amplitude noise occur. (b) Shifting of observing view due to outside impulse and incorrect recognition of non-existing droplet jumping events. (c) Raw data for

recognized droplet number and weight with respect to frame number after deleting the frames with high spike.

The second factor is low amplitude noise caused by random vibration during the condensation experiments (e.g. vibration the cooling system, people walking around). As illustrated in Figure S11a, the image recognition algorithm would detect circles between two frames without any droplet jumping event. Thirdly, due to air turbulence, some removed droplets would jump back to the vertically oriented surfaces, which cannot be recognized using forward subtraction since now droplet in frame 2 is brighter than the darker background in frame 1, as shown in Figure S11b. Furthermore, not all the coalesced droplets can experience self-propelled jumping, some of the droplets coalesce without being removed from the surface, which can be clearly seen in Figure S11c and S11d, where one is coalescence-induced sliding and the other is immobile coalescence.

Herein, reverse subtraction, which subtracts frame 2 by frame 1 can be employed to partially eliminate the factors affecting accuracy of the image recognition algorithm. In terms of droplets jumping into the observing view, as well as coalesced sliding events, reverse subtraction can recognize them in a similar fashion as forward subtraction for removed droplets, so the effects would cancel out, as shown in Figure S11b and S11c. Less accurately, reverse subtraction can partially account for immobile coalescing events. For instance, as shown in Figure S11d, the recognized weight amount of “droplet out” (0.071 g/m^2) through forward subtraction can be partly accounted by recognized weight account “droplet in” (0.091 g/m^2) through reverse subtraction.

Lastly, low amplitude noise recognized through reverse subtraction should be similar to forward subtraction, as the amplitude of the random vibration is the same. Although not perfect, reverse subtraction does lower the discrepancy between image recognition algorithm and manual counting from $29.6\pm 18.8\%$ to $7.4\pm 5.3\%$ (Table S1).

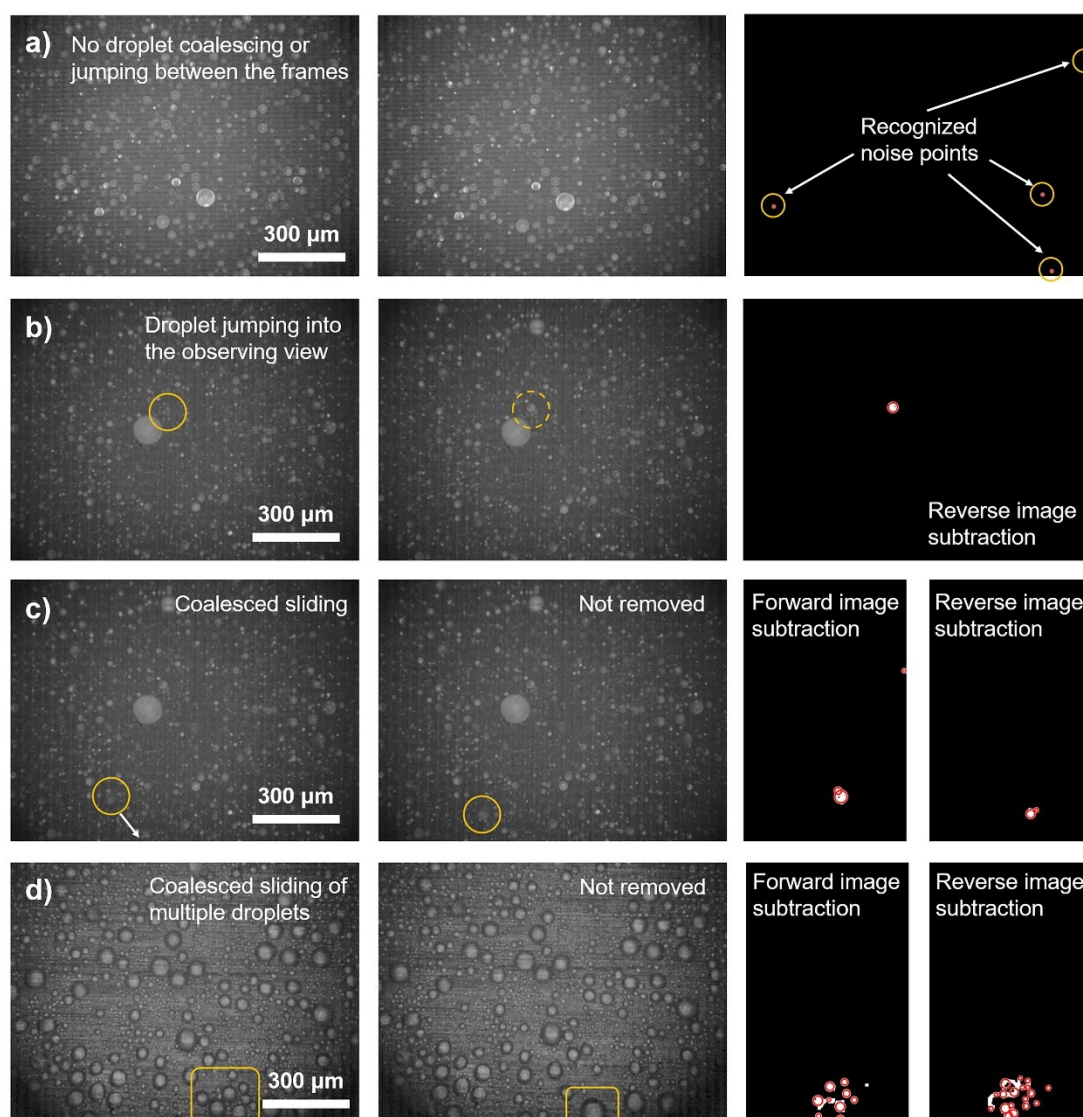


Figure S11. Factors affecting the accuracy of image recognition algorithm. (a) Low amplitude noise caused by random vibration. (b) Droplet jumping into the frame. (c) Coalesced droplets slide in the observing without being removed. (d) Immobile coalescence.

There are also a few other things to be considered. From analyzing the recorded videos frame by frame, it is generally true that coalesced droplets would jump on MCS with higher probability once it suspend on top the micro-cone structure than can NS due to the fact that coalesced droplets on MCS having higher mobility even for large size mismatch (M), as illustrated in Figure S12a-b, where the values for M are 2.4 and 2.8, respectively. And since our image recognition algorithm is less accurate in dealing with immobile coalescence even after incorporating reverse subtraction, the accuracy of results should decrease for surfaces with higher adhesion (e.g. on NS surfaces). In addition, it should be noted that amount of water removal for the SHSs should not be compared for time duration as short as 100 frames (10 s), as an occasional large droplet jumping might occur, which significantly increases amount of water removal, as illustrated in Figure S12c. Moreover, light reflect on droplet differently for NS than on MCS, the outer edges of the otherwise bright droplets are dimmer than the substrate (Figure S12d), so the diameters of the recognized droplets were further multiplied by 1.25 to obtain the correct value. Lastly, to obtain results comparable to careful manual counting, tremendous efforts were dedicated to fine-tuning parameters such as image thresholding limit, circle detection sensitivity, edge detection sensitivity etc. However, more work is required to further improve accuracy of the results (e.g. employ experimental setup with higher resolution and image contrast; eliminate random noise; develop an algorithm that recognizes immobile coalescence and disregard it completely, rather than through reverse subtraction).

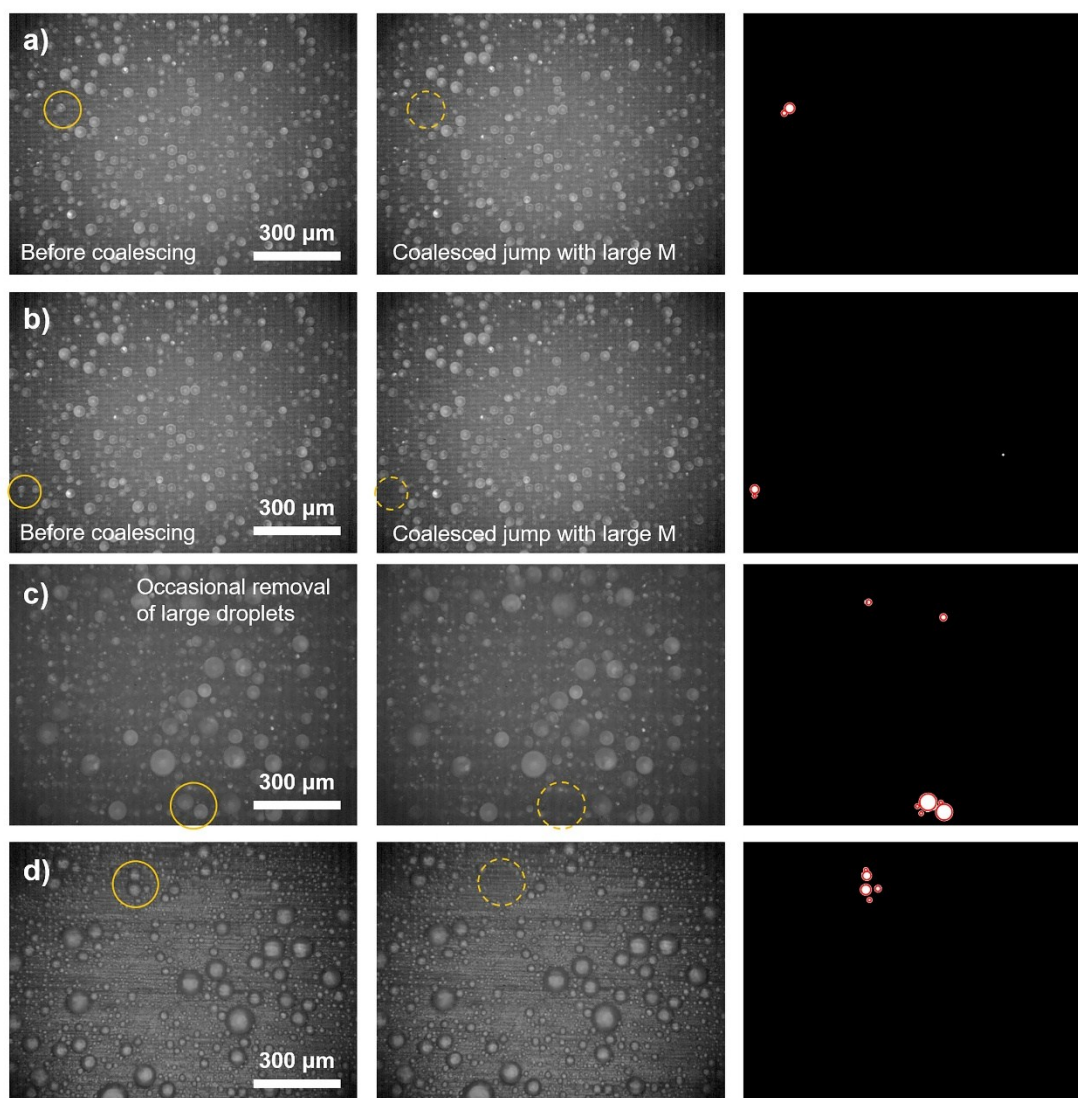


Figure S12. Some other consideration for image recognition algorithm. (a)-(b) Coalesced droplets suspending on micro-cones can jump on MCS20 surfaces even with large droplet size mismatch. Immobile coalescence events were less likely to occur on MCS than on NS. (c) Removal of large droplets can significantly affect droplet weight calculation for short time duration. (d) Removed droplet diameter on NS should multiply by 1.25 since the outer edge of the bright droplet is dimmer than the substrate.

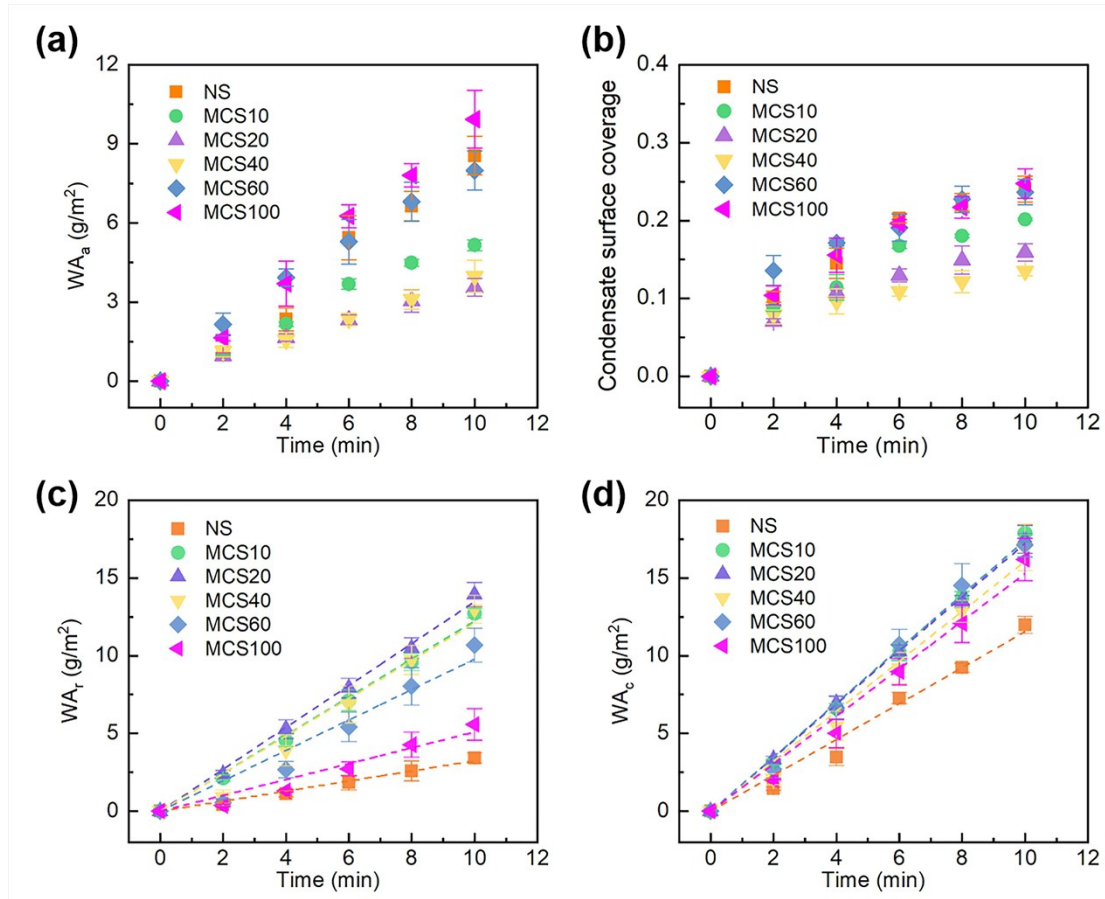


Figure S13. Statistical results of the 10 minutes condensation process for the SHSs. (a) Amount of accumulated water per unit area with respect to time. (b) Condensate area coverage with respect to time. (c) Amount of removed water per unit area through self-propelled jumping, the trends are linear with respect to time as illustrated by the fitted dash lines. (d) Amount of condensed water per unit area, which is calculated by summing the accumulated and removed water amount. The trends are also linear, and water removing efficiency can be calculated by $E_{wr} = WA_r/WA_c$.

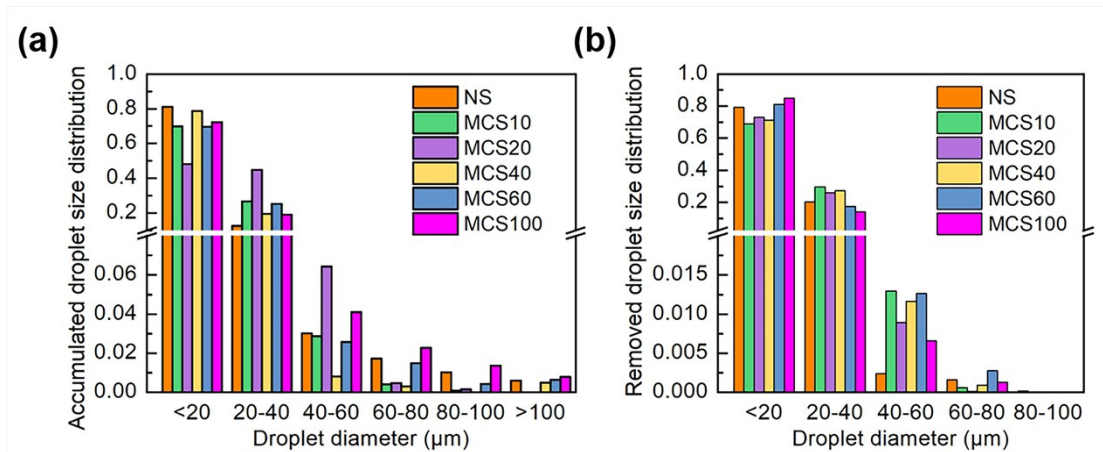


Figure S14. Size distribution for (a) accumulated droplets and (b) removed droplets, for the prepared samples.

S4. Partial Wetting of Condensed Droplets, Experiments and Theory

Experimental results (Figure S15a-b) show that two droplets coalescing in Cassie state on NS and MCS surfaces have indistinguishable jumping velocity, which disagrees with the condensing experiment results. The droplet jumping experiment is conducted at room temperature using the same method adopted by Yan et al.² (see Experimental section for details). During the droplet jumping experiments, the radii of the binary droplets were changed while the droplet size ratio M was kept at $M = 1$ and $M = 1.5$, respectively. Here, the droplet mismatch M is defined as the ratio between the larger droplet to the smaller droplet before coalescence.²

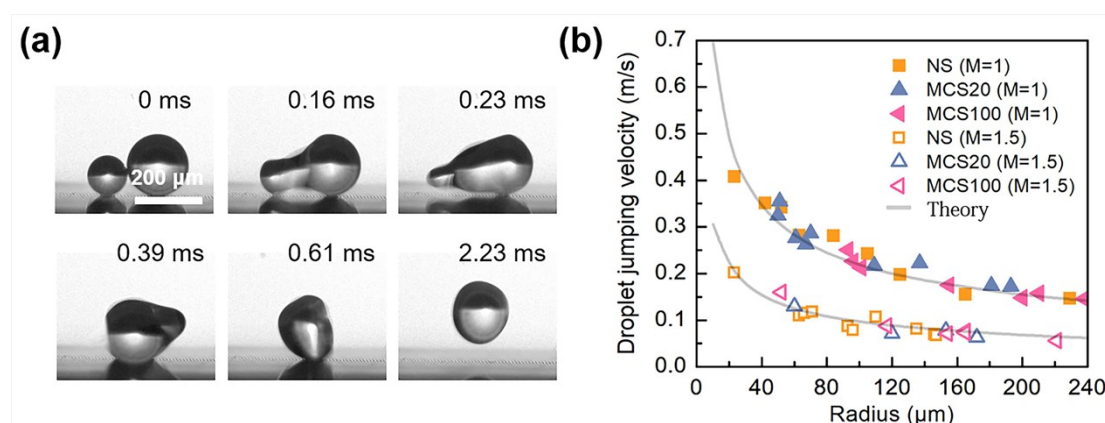


Figure S15. Coalesced jumping of droplets in Cassie state. (a) Illustration of the coalesced jumping process of droplets with $M = 1.5$. (b) Experimental and theoretical jumping velocities of NS, MCS20 and MCS100.

Released surface energy. The droplet jumping experimental results can be analyzed theoretically to provide insights into how different factors would influence droplet jumping capability. It is usually taken that v needs to be greater than 0.05 m/s for coalesced droplet to jump off the surface. The velocity (v) of the jumping droplet can be calculated as:

$$v = \sqrt{\frac{2E_k}{m}} > 0.05 \text{ m/s}, \quad (\text{S1})$$

where

$$E_k = \eta \Delta E_s - E_{ad} - E_g. \quad (\text{S2})$$

The coalescence-induced droplet jumping event can be divided into three states, namely, before coalescing (State 1), during coalescing (State 2) and coalesced jump (State 3), as shown in Figure S16.³ The released surface energy from the coalescence event can be then calculated by taking the difference in total surface area between State 1 and State 3 and multiply it by the surface tension of water σ_{lv} :

$$\Delta E_s = E_{s,1} - E_{s,3}, \quad (\text{S3})$$

where

$$E_{s,1} = \sum (\sigma_{lv} A_{1,i,lv} - \sigma_{lv} A_{1,i,sl} \cos \theta_{app}), \quad (\text{S4})$$

$$E_{s,3} = \sigma_{lv} A_{3,lv}, \quad (\text{S5})$$

where $A_{1,i,lv}$ and $A_{1,i,sl}$ represent the liquid-vapor and solid-liquid contact area of the droplets in State 1, respectively. $A_{3,lv}$ is the liquid-vapor contact area of the final jumped droplet in State 3 and θ_{app} is the apparent static contact angles of the droplets.

From Figure S16,

$$A_{1,i,lv} = 2\pi R_{1,i}^2 (1 - \cos \theta_{app}) + (1 - \varphi)\pi R_{1,i}^2 \sin^2 \theta_{app}, \quad (\text{S6})$$

$$A_{1,i,sl} = \varphi\pi R_{1,i}^2 \sin^2 \theta_{app}, \quad (\text{S7})$$

$$A_{3,lv} = 4\pi R_3^2, \quad (\text{S8})$$

$$R_3 = \left(\frac{3 \sum V_{1,i}}{4\pi} \right)^{1/3}, \quad (\text{S9})$$

$$V_{1,i} = \frac{\pi}{3} R_{1,i}^3 (2 + \cos \theta_{app}) (1 - \cos \theta_{app})^2, \quad (\text{S10})$$

where $R_{1,i}$ and φ are radii of the droplets in State 1 and solid fraction between the droplets and the surface. R_3 is the radius of the jumped droplet in State 3. And $V_{1,i}$ is the volume of the droplets in State 1.

By combining Equation S3 through S10, the released surface energy from coalescing droplets is:

$$\begin{aligned} \Delta E_s &= \sum \left[2\sigma_{lv}\pi R_{1,i}^2 (1 - \cos \theta_{app}) + (1 - \varphi)\pi R_{1,i}^2 \sin^2 \theta_{app} - \sigma_{lv}\varphi\pi R_{1,i} \right. \\ &\quad \left. - \sigma_{lv}4\pi \left(\frac{\sum [\pi R_{1,i}^3 (2 + \cos \theta_{app}) (1 - \cos \theta_{app})^2]}{4\pi} \right)^{2/3} \right]. \end{aligned} \quad (\text{S11})$$

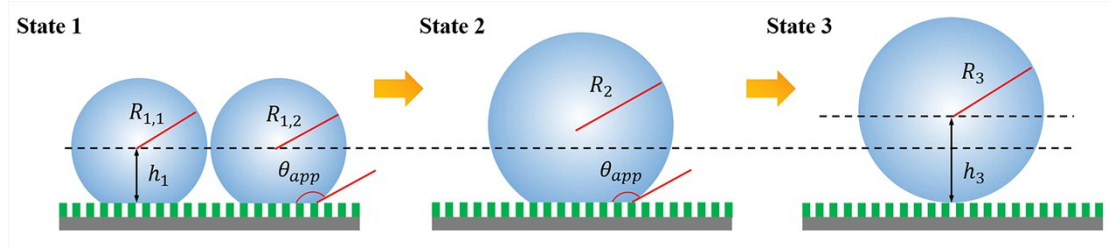


Figure S16. Schematic illustration shows the droplet jumping process through coalescence.

It is experimentally observed that for coalesced droplets, most of the released surface energy are dissipated, and only a small fraction ($< 6\%$) of it is converted into kinetic energy for droplet to jump, and the dissipation factor η is can be expressed as:²

$$\eta = \frac{0.056}{1 + 33.6\chi^2} e^{-4.41\chi^2}, \quad (\text{S12})$$

where χ is the normalized droplet size mismatch defined as $(R_{1,1} - R_{1,2})/(R_{1,1} + R_{1,2})$ for two-droplet coalescence.

Adhesion between the droplets and the surface in Cassie state. Coalesced droplet jumping requires the released surface energy to overcome the surface adhesion. When the coalescing droplets are initially in Cassie state (Figure S17a), the total adhesion energy (E_{ad}) can be calculated as:⁴

$$E_{ad} = E_{ad,1-2,cassie} + E_{ad,2-3}, \quad (S13)$$

$$E_{ad,1-2,cassie} = \sum A_{1,i,sl} \sigma_{lv} (1 + \cos \theta_{rec,cassie}), \quad (S14)$$

$$E_{ad,2-3} = A_{2,sl} \sigma_{lv} (1 + \cos \theta_{rec,cassie}), \quad (S15)$$

where $E_{ad,1-2,cassie}$ and $E_{ad,2-3}$ are adhesion energy from State 1 to State 2, and from State 2 to State 3, respectively. $\theta_{rec,cassie}$ is the receding contact angle of the droplets.

Moreover, from Figure S17a:

$$A_{1,i,sl} = \varphi R_{1,i}^2 (\pi \sin^2 \theta_{app}), \quad (S16)$$

$$A_{2,sl} = \varphi R_2^2 (\pi \sin^2 \theta_{app}), \quad (S17)$$

$$R_2 = \left(\frac{3 \sum V_{1,i}}{(2 + \cos \theta_{app})(1 - \cos \theta_{app})^2} \right)^{1/3}, \quad (S18)$$

where R_2 is the radius of the coalesced droplet at State 2. By combining Equation S13 through S18, the adhesion energies for droplets with initial Cassie state between State 1 to State 2 and State 2 to State 3 are:

$$E_{ad,1-2,cassie} = \sum [\varphi R_{1,i}^2 (\sigma_{lv} \pi \sin^2 \theta_{app} (1 + \cos \theta_{rec,cassie}))], \text{ and } \quad (S19)$$

$$E_{ad,2-3} = \varphi \sigma_{lv} \pi \sin^2 \theta_{app} (1 + \cos \theta_{rec,cassie})$$

$$\times \left(\frac{\sum [\pi R_{1,i}^3 (2 + \cos \theta_{app}) (1 - \cos \theta_{app})^2]}{(2 + \cos \theta_{app}) (1 - \cos \theta_{app})^2} \right)^{2/3}.$$

(S20)

Adhesion between the droplets and the surface in PW state. When initial coalescing droplets are in PW state, the adhesion of droplets in State 1 ($E_{ad,1-2,pw}$) can be divided into $E_{ad,1-2,nw}$ (adhesion with respect to the non-wetting part of the droplet-surface interface), and $E_{ad,1-2,w}$ (adhesion with respect to the wetted part of the droplet-surface interface) to account for the adhesion energy induced by wetting of surface structures, expressed as:

$$E_{ad} = E_{ad,1-2,pw} + E_{ad,2-3} = E_{ad,1-2,nw} + E_{ad,1-2,w} + E_{ad,2-3} \quad (S21)$$

The non-wetting adhesion $E_{ad,1-2,nw}$ at the droplet surface interface can be calculated by changing the contact angle in Equation S19 from $\theta_{rec, cassie}$ to $\theta_{rec, pw}$, as illustrate in Figure S17b:

$$E_{ad,1-2,nw} = \sum [\varphi R_{1,i}^2 (\sigma_{lv} \pi \sin^2 \theta_{app} (1 + \cos \theta_{rec,pw}))], \quad (S22)$$

Since the solid fraction term φ is defined as the fraction of solid-liquid contact area to the apparent droplet-surface contact area, the term $(1 - \varphi)$ then represents the liquid-vapor contact area when the droplet suspends on top of the nanostructures in Cassie state. However, for PW state, a fraction of the liquid-vapor contact area is now replaced by contact between the droplet and water bridges within the surface nanostructure, and additional adhesion term for the partially wetted region ($E_{ad,1-2,w}$) needs to be incorporated to the total adhesion $E_{ad,1-2,pw}$ in State 1:

$$E_{ad,1-2,w} = \sum [(1 - \varphi) \phi_{pw} R_{1,i}^2 (\sigma_{lv} \pi \sin^2 \theta_{app} (1 + \cos \theta_w))], \quad (S23)$$

where ϕ_{pw} is the degree of partial wetting, as illustrated in Figure 5b, and θ_w is the contact angle between the droplet and water bridges within the nanostructures, which is just 0° .

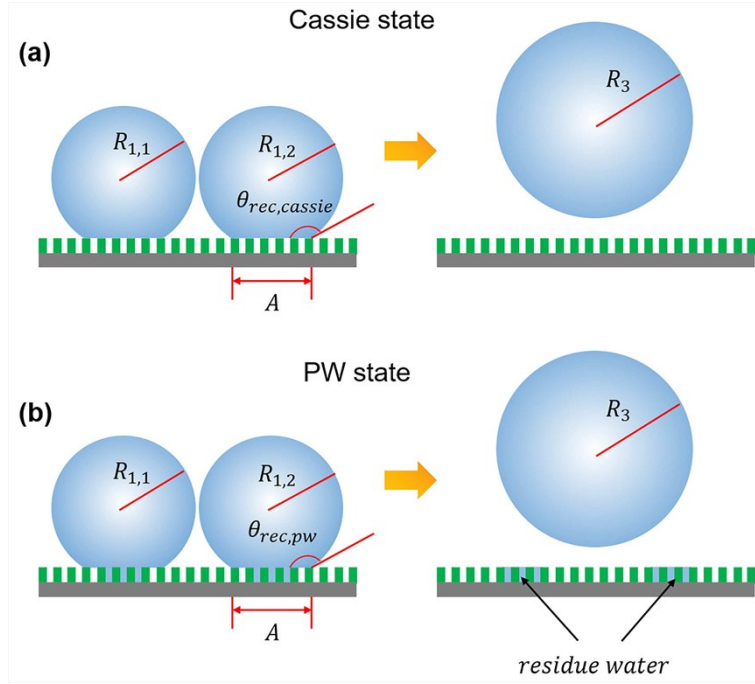


Figure S17. Schematic illustration show adhesion need to be overcome when initial droplet wetting states are in (a) Cassie state, and (b) PW state.

Gravity. Lastly, from Figure S16, the gravitational energy can be calculated as:⁵

$$\Delta E_g = mg(h_3 - h_1), \quad (\text{S24})$$

where

$$h_1 = \frac{R_1(3 + \cos \theta_{app})(1 - \cos \theta_{app})}{4(2 + \cos \theta_{app})}, \quad (\text{S25})$$

$$h_3 = R_3 = R_1 \frac{(2 - 3\cos \theta_{app} + \cos^3 \theta_{app})^{1/3}}{2}, \quad (\text{S26})$$

By combining Equation S24 through S26,

$$\Delta E_g = \frac{4}{3}\pi R_1^4 \rho g \left[\frac{(2 - 3\cos \theta_{app} + \cos^3 \theta_{app})^{1/3}}{2} - \frac{(3 + \cos \theta_{app})(1 - \cos \theta_{app})}{4(2 + \cos \theta_{app})} \right],$$

(S27)

Limitations for the proposed energy analysis. Since this work is not focused on establishing a concrete mechanism analysis for coalesced droplet jumping in PW state based on experimental results, but rather to provide framework for future analysis, the parameters such as contact angles and solid fraction were not directly measured. Therefore, experimental results from previous works are taken to demonstrate the effect of different parameters on water removal capability through droplet jumping.^{2, 6, 7} Moreover, according to the analysis, the degree of partial wetting significantly influences droplet jumping capability, but the exact value cannot be measured directly. Furthermore, the assumption where the coalesced droplet in State 2 is in Cassie state might not be correct, as there might be presence of liquid-bridge within the nanostructure at the coalescing spot in State 2. Other than the hierarchical micro-cone, nano-blade structure, the prepared samples exhibit a micro-roughness of 1-2 μm due to laser processing, which is not accounted in the theoretical analysis, and the effect of this roughness is currently unknown. In general, more experiments are required to consolidate the theoretical analysis proposed in this work, where the jumping velocity of PW droplets should be accurately measured with respect to given parameters (e.g. degree of partial wetting).

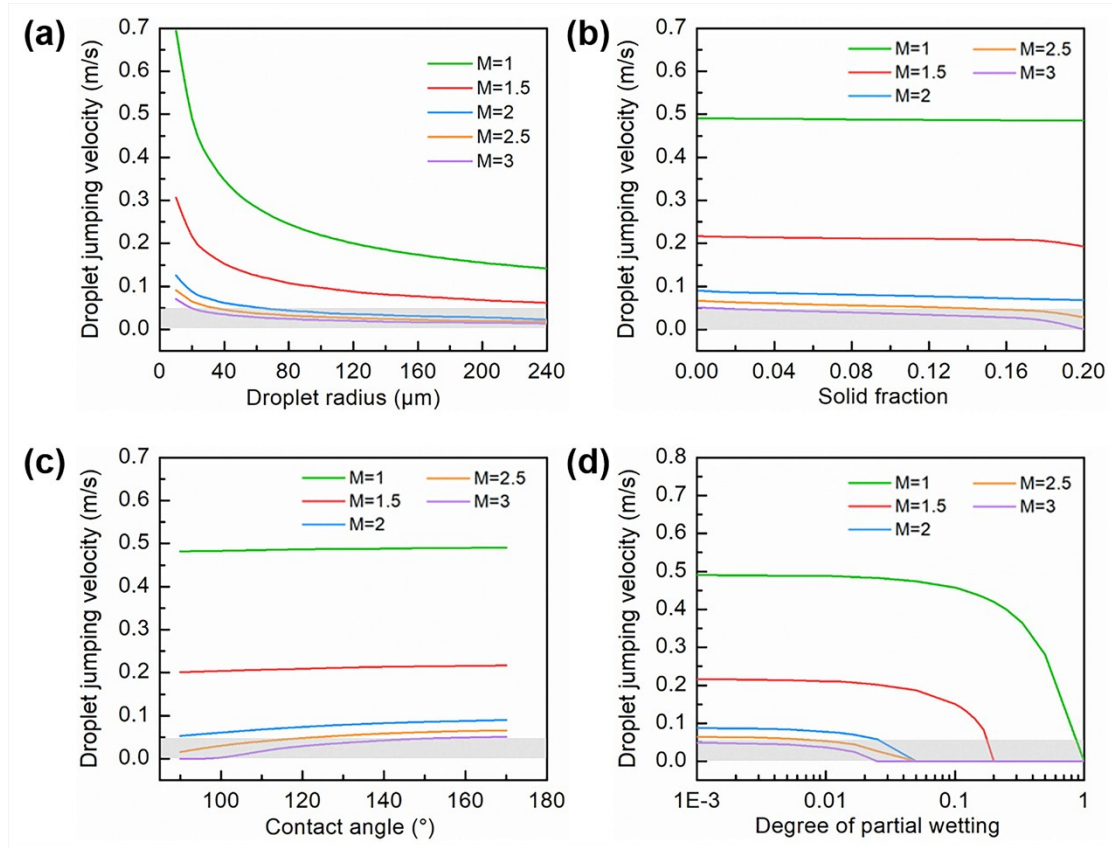


Figure S18. Theoretical analysis of droplet jumping velocity in a two-droplets system with respect to different influences. (a) High M and large droplet size lead to reduced jumping velocity of the coalesced droplets ($\varphi = 0.02$, $\theta_{rec} = 160^\circ$, $\phi_{pw} = 0$). (b) Solid fraction generally has less effect for droplet jumping velocity when considering NS ($\varphi_n \sim 0.02$ -0.2) and MCS ($\varphi_{mn} < 0.02$). Effects are only noticeable for $M > 2$ (20 μm diameter for the smaller droplet, $\theta_{rec} = 160^\circ$, $\phi_{pw} = 0$). (c) Jumping velocity increases for higher receding contact angle (θ_{rec}), but the effect is in general quite small (20 μm diameter for the smaller droplet, $\varphi = 0.02$, $\phi_{pw} = 0$). (d) The presence of partial wetting (ϕ_{pw}) is the primary factor that determines droplet-surface adhesion and consequently jumping velocity of coalesced droplets (20 μm diameter for the smaller droplet, $\varphi = 0.02$, $\theta_{rec} = 160^\circ$).

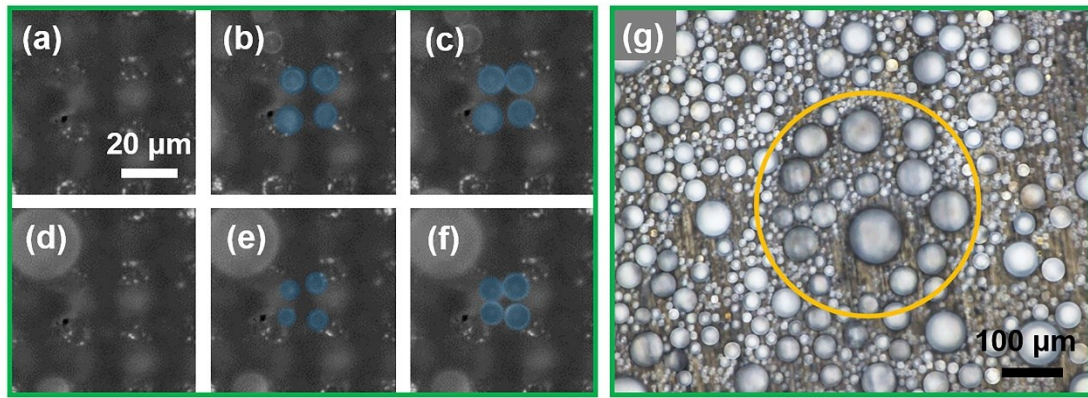


Figure S19. Evidence of partial wetting. (a)-(f) The droplets are more likely to condense and grow on spots where droplets just coalesced and jumped away, indicating possible wetted patches at these spots, which provides nucleation sites for condensed droplets. (g) Droplets on nanostructured surface sometimes do not retain spherical shape under high supersaturation and high supercooling, indicating some of them completed wetted the surface nanostructure.

S5. Partial Wetting State to Cassie State Transition

From Yan et al. and Sharma et al., the outward motion of a droplet within the reverse cone-shape diverging track with a taper angle of 2α (self-transport) can be achieved when $F_l \geq F_g + F_f$, where F_l is the outward force induced by Laplace pressure gradient, and F_g and F_f are gravitational and the friction force induced by capillarity, respectively, as schematically illustrated in Figure S20a.^{8,9}

The pressure difference between the outside (P_o) and the inside ($P_{in,u}$, $P_{in,l}$) of the upper and lower menisci can be estimated by the Young-Laplace equation:

$$\Delta P_{in} = \Delta P_{in,u} - \Delta P_{in,l} \quad (\text{S28})$$

where

$$\Delta P_{in,u} = P_{in,u} - P_o = \frac{2\sigma_{lv}}{R_u}, \quad (\text{S29})$$

$$\Delta P_{in,l} = P_{in,l} - P_o = \frac{2\sigma_{lv}}{R_l}, \quad (\text{S30})$$

where R_u is the curvature radius corresponding to the upper interface, and R_l is the curvature radius corresponding to the lower interface;

Based on Figure S20a, the radii of curvature for the upper and lower menisci are calculated as:

$$R_u = -\frac{H_u \sin \alpha}{\cos \theta_u}, \quad (\text{S31})$$

$$R_l = -\frac{H_l \sin \alpha}{\cos \theta_l}, \quad (\text{S32})$$

where H_u is the height of the circle center corresponding to the upper interface and H_l is the height of the sphere center corresponding to the lower interface, which is also

defined as the initial position of the condensed droplet. $\theta_u = \theta_{adv} = 170^\circ$ (typical advancing contact angle at the upper interface for condensed microdroplets), $\theta_l = \theta_{rec}$ (receding contact angle at the lower interface) and $\alpha = 37.6^\circ$.

The net outward force can then be estimated by integrating the pressure gradient over the volume Ω :

$$F_l = \iiint \nabla P_{in} d\Omega' \approx \frac{\Delta P_{in}}{\Delta h} \Omega_t, \quad (S33)$$

where the volume of the condensed droplet is calculated as:

$$\Omega_t = \Omega_u + \Omega_l + \Omega_m, \quad (S34)$$

$$\Omega_m = \frac{1}{3}\pi r_u^2 h_u - \frac{1}{3}\pi r_l^2 h_l, \quad (S35)$$

$$\Omega_u = \frac{1}{3}\pi r_u^3 [2 - 3\sin(\theta_u + \alpha) + \sin^3(\theta_u + \alpha)], \quad (S36)$$

$$\Omega_l = \frac{1}{3}\pi r_l^3 [2 - 3\sin(\theta_l - \alpha) + \sin^3(\theta_l - \alpha)], \quad (S37)$$

where Ω_t , Ω_u , Ω_l , and Ω_m are the total volume, the volume of the upper spherical cap, the volume of the lower spherical cap, and the volume of the middle section between the upper and lower spherical cap, respectively. and

$$r_u = -R_u \cos(\theta_u + \alpha), \quad (S38)$$

$$r_l = -R_l \cos(\theta_l + \alpha), \quad (S39)$$

$$h_u = H_u + R_u \sin(\theta_u + \alpha), \quad (S40)$$

$$h_l = H_l - R_l \sin(\theta_l - \alpha), \quad (S41)$$

where r_u and r_l are the radii of the upper and lower spherical cap, respectively. h_u and h_l are the heights of the upper and lower spherical cap base.

The gravitational force acting on the condensed droplet can then be calculated as:

$$F_g = \rho \Omega_t g, \quad (\text{S42})$$

The frictional force resulting from capillarity can be obtained by assuming symmetrical geometry at the upper and lower triple phase contact line. For simplicity, the upper and bottom contact lines are assumed to be circular, and the net frictional force can be estimated as:

$$F_f = F_{f,l} + F_{f,u} = 2\pi\sigma_{lv}\cos\alpha(r_l\cos\theta_l - r_u\cos\theta_u), \quad (\text{S43})$$

Herein, the critical droplet diameter for self-transport within the reverse cone track ($F_l \geq F_g + F_f$) is defined as $d_{crit} = d_u(\theta_u, \theta_l, \alpha, H_u) = 2r_u(\theta_u, \theta_l, \alpha, H_u)$ for a given receding contact angle. By setting $\theta_u = \theta_{adv} = 170^\circ$, $\alpha = 37.6^\circ$ (for the structured micro-cones in this work) and $H_u = 5 \mu\text{m}$, d_{crit} for $\theta_l = \theta_{rec}$ between 95° - 170° can be calculated, and is shown in Figure S20b. For instance, at a θ_{rec} of 160° , d_{crit} is around $12 \mu\text{m}$, which can be interpreted as the minimum droplet size required for the growing droplet to experience net outward force.

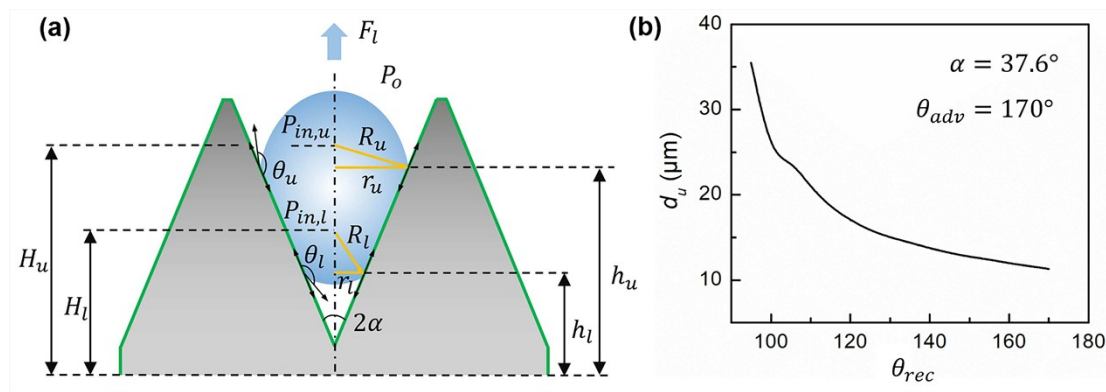


Figure S20. Force analysis of the growing condensed droplet within the reverse cone-shape diverging track. (a) 2D geometrical configuration of a growing condensed droplet within a reverse cone track. (b) Critical droplet diameter for self-transport (d_{crit}) for PW

to Cassie transition to occur at a given receding contact angle.

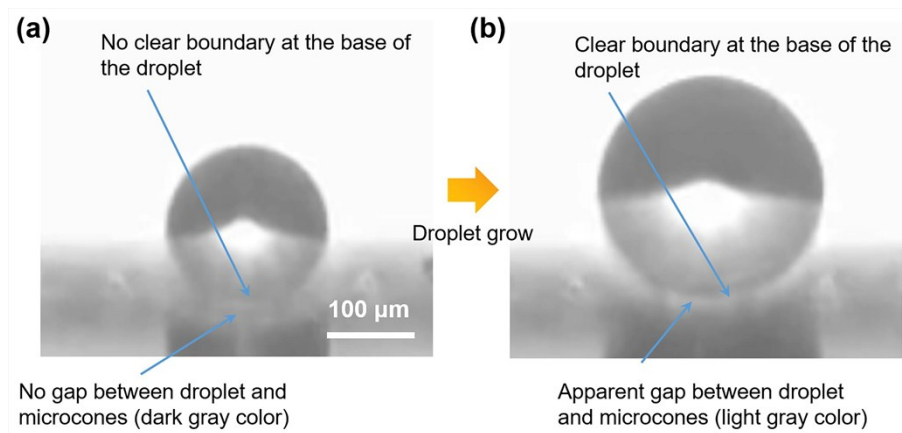


Figure S21. Illustration of a microdroplets growing within the micro-cones and eventually suspending on top of them, as indicated by the gap between the structured surface and the lower boundary of the droplet.

S6. Frosting Experiment.

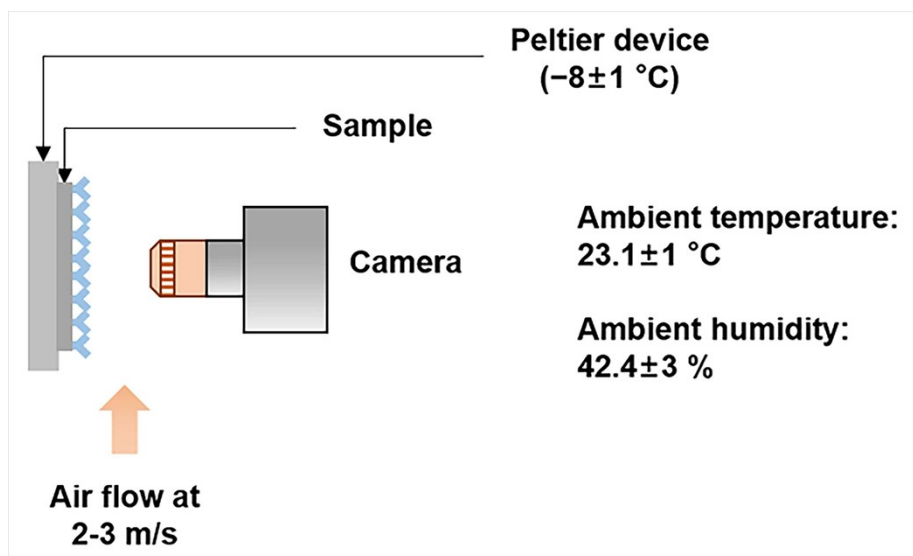


Figure S22. Schematic illustration of the setup for the frosting experiments.

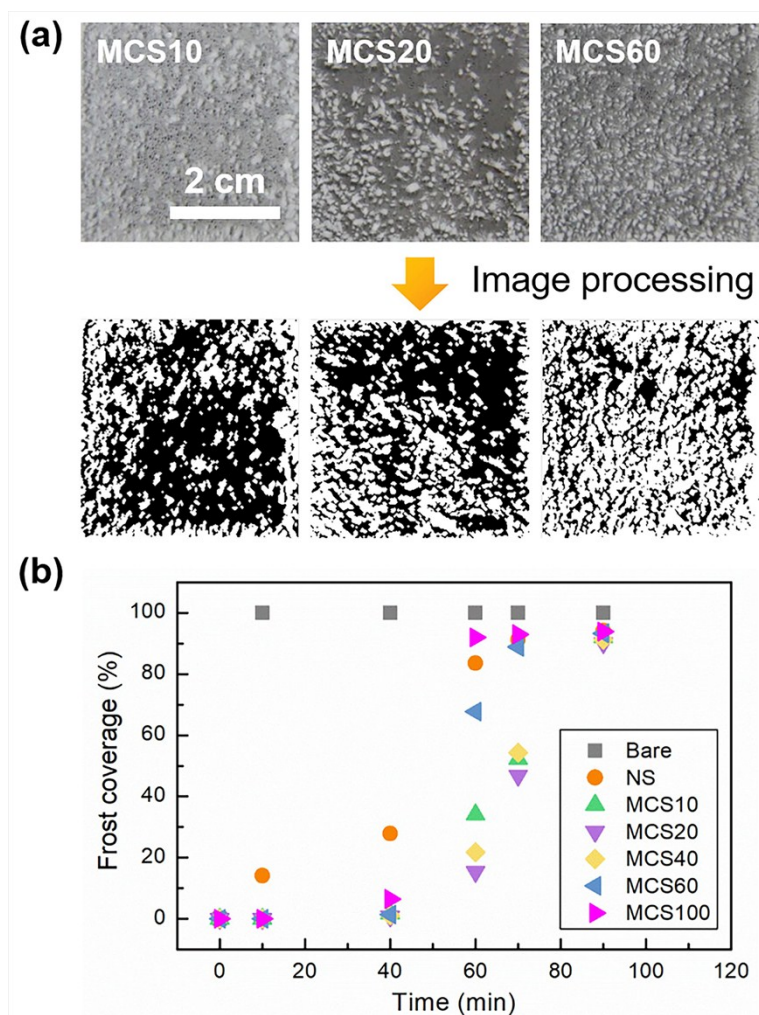


Figure S23. Frost coverage of the prepared samples. (a) Representative images show that the fraction of frost (white) to surface (black) can be estimated from an image processing and pixel counting algorithm using MATLAB. (b) Frost coverage over time for the prepared samples.

S7. Supporting Figures for the Discussion Section

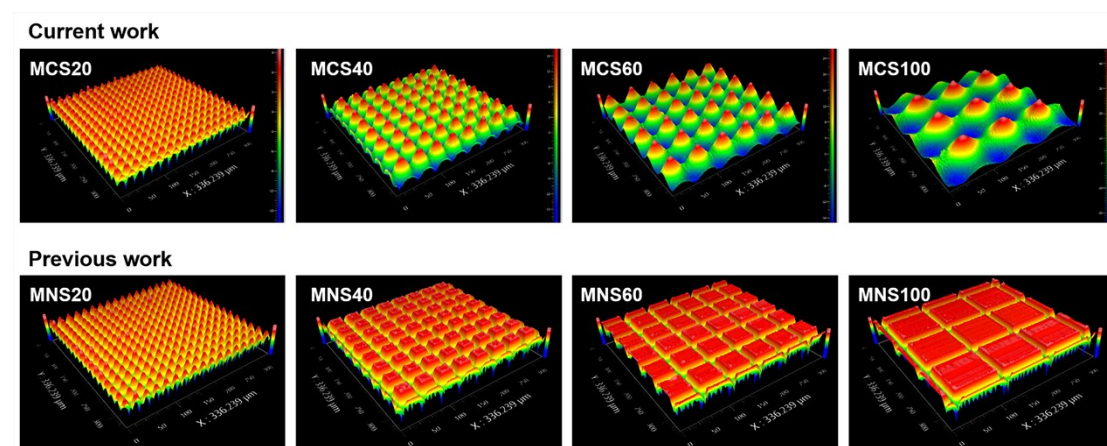


Figure S24. White-light interferometry images shows the difference in surface morphology of the prepared SHSs between this and the previously published work.¹⁰

Supporting references

1. M. Malinauskas, A. Žukauskas, S. Hasegawa, Y. Hayasaki, V. Mizeikis, R. Buividas and S. Juodkasis, *Light: Science & Applications*, 2016, **5**, e16133.
2. X. Yan, L. Zhang, S. Sett, L. Feng, C. Zhao, Z. Huang, H. Vahabi, A. K. Kota, F. Chen and N. Miljkovic, *ACS Nano*, 2019, **13**, 1309-1323.
3. H. Cha, C. Xu, J. Sotelo, J. M. Chun, Y. Yokoyama, R. Enright and N. Miljkovic, *Physical Review Fluids*, 2016, **1**, 064102.
4. M. He, X. Zhou, X. Zeng, D. Cui, Q. Zhang, J. Chen, H. Li, J. Wang, Z. Cao, Y. Song and L. Jiang, *Soft Matter*, 2012, **8**, 6680-6683.
5. K. Wang, Q. Liang, R. Jiang, Y. Zheng, Z. Lan and X. Ma, *RSC Advances*, 2016, **6**, 99314-99321.
6. R. Enright, N. Miljkovic, A. Al-Obeidi, C. V. Thompson and E. N. Wang, *Langmuir*, 2012, **28**, 14424-14432.
7. H. Cha, J. Ma, Y. S. Kim, L. Li, L. Sun, J. Tong and N. Miljkovic, *ACS Nano*, 2019, **13**, 13343-13353.
8. X. Yan, F. Chen, S. Sett, S. Chavan, H. Li, L. Feng, L. Li, F. Zhao, C. Zhao, Z. Huang and N. Miljkovic, *ACS Nano*, 2019, **13**, 8169-8184.
9. C. S. Sharma, C. Stamatopoulos, R. Suter, P. R. von Rohr and D. Poulikakos, *ACS Applied Materials & Interfaces*, 2018, **10**, 29127-29135.
10. G. Zhao, G. Zou, W. Wang, R. Geng, X. Yan, Z. He, L. Liu, X. Zhou, J. Lv and J. Wang, *ACS Applied Materials & Interfaces*, 2020, DOI: 10.1021/acsami.9b21704.